

Assessments of land subsidence along Rizhao-Lankao High-speed Railway at Heze, China between 2015 and 2019 with Sentinel-1 data

Chuanguang Zhu¹, Wenhao Wu¹, Mahdi Motagh^{2,3}, Liya Zhang¹, Zongli Jiang¹, and Sichun Long¹

¹Key Laboratory of Coal Resources Clean-utilization & Mine Environment Protection of Hunan Province, Hunan university of Science & Technology, Xiangtan 411201, China

²Section of Remote Sensing and Geoinformatics at GFZ German Research Centre for Geosciences in Potsdam, Germany

³Institute of Photogrammetry and Geoinformation at Leibniz University Hannover (LUH) in Hannover, Germany

Correspondence to: Chuanguang Zhu (zhucg@hnust.edu.cn)

Abstract. The Heze section of Rizhao-Lankao High-speed Railway (RLHR-HZ) has been under construction since 2018 and will be operative by the end of 2021. However, there is a concern that land subsidence in Heze region may affect the regular operation of RLHR-HZ. In this study, we investigate the contemporary ground deformation in the region between 2015 and 2019 by using more than 350 C-band interferograms constructed from two tracks of Sentinel-1 data over the region. The Small Baselines Subset (SBAS) technique is adopted to compile the time series displacement. We find that the RLHR-HZ runs through two main subsidence areas: one is located east of Heze region with rates ranging from -4 cm/yr to -1 cm/yr, and another one is located in the coalfield with rates ranging from -8 cm/yr to -2 cm/yr. A total length of 35 km of RLHR-HZ is affected by the two subsidence basins. Considering the previous investigation and the monthly precipitation, we infer that the subsidence bowl east of Heze region is due to massive extraction of deep groundwater. Close inspections of the relative locations between the second subsidence area and the underground mining reveals that the subsidence there is probably caused by the groundwater outflow and fault instability due to mining, rather than being directly caused by mining. The InSAR-derived ground subsidence implies that it's necessary to continue monitoring the ground deformation along RLHR-HZ.

1 Introduction

The Heze region, lying in the North China Plain, has been adversely affected for decades by ground subsidence, mainly caused by the soil compaction and consolidation due to the excessive exploitation of aquifer (Cui 2018; Hu et al., 2004; Guo et al., 2019; Xue et al., 2005). To slow down the subsidence, the local governments have proposed new regulations on exploitation of groundwater. However, groundwater extraction is still greater than recharge due to the urban sprawl and industrial development, which results in continuous ground subsidence. In addition, underground mining activities have also exacerbated the problems of subsidence in recent years (Wang 2014; Yang et al., 2010). The resulting subsidence has

1 already caused some environment hazards, e.g., collapse of roads, buildings and other infrastructures (Yue
2 2020).

3 The RLSR-HZ, with a length of 150 km and a speed of 300 kph, has been under construction since
4 December 2018 and will be operative by the end of 2021. The ground subsidence may menace the
5 RLSR-HZ and therefore currently is a matter of major safety concern. It is crucial to monitor ground
6 deformation along the RLSR-HZ to avoid potential hazards in the future.

7 Field-survey based on a few sparse points, such as spirit leveling and global position system (GPS), is
8 the main methods for measuring ground deformation in Heze region. However, it is difficult to obtain
9 detailed and comprehensive deformation based on these sparse points. Moreover, these geodetic
10 measurements are very time-consuming and highly labor intensive, especially for the RLSR-HZ extending
11 over a large region. More advanced methods are required to retrieve the latest temporal and spatial
12 evolution of ground deformation along the RLSR-HZ.

13 Utilizing the conjugate product (i.e., interferogram) of two co-registered SAR images, Interferometric
14 Synthetic Aperture Radar (InSAR) can remotely map the ground deformation over a large area (Gabriel et
15 al., 1989; Massonnet and Feigl 1998). However, several factors such as atmospheric effect, orbit and
16 topography error and other noise, limit the accuracy of InSAR. Multi-temporal InSAR (MT-InSAR), such
17 as Persistent Scatter Interferometry (PSI) (Ferretti et al., 2000, 2001; Hooper et al., 2007; Kampes, 2006)
18 and Small Baseline Subset (SBAS) algorithm (Berardino et al., 2002; Hooper 2008; Mora et al., 2003), is
19 introduced to overcome these limitations by utilizing the pixels that contain coherent information in a
20 time-series co-registered SAR images. In recent years, MT-InSAR plays an important role in mapping
21 ground deformation with high precision and spatial resolution over a large area (André 2016; Du et al.,
22 2018; Haghighi et al., 2019; Miller and Shirzaei 2019; Motagh et al., 2017; Zhang et al, 2019).

23 Generally, PSI is suitable in urban areas where many human-made structures provide the vast majority of
24 PSs. However, most of the area, running through by RLSR-HZ, is covered by farmlands, which leads to a
25 low density of PSs. Distributed scatterers (DSs), also referred as Gaussian scatterers with random scattering
26 mechanism (Bamler and Hart, 1998; Goodman, 1976), are widespread in natural scene and can be used in
27 SBAS method to increase the density of measurement points (Hooper 2008; Samiei-Esfahany 2017).
28 SqueeSAR (Ferretti et al., 2011) is another advanced approach, that allows us to extract the signal from
29 both PS and DS. SqueeSAR extracts information by exploiting all the possible interferograms rather than a
30 set of SBAS interferograms (Ferretti et al., 2011; Samiei-Esfahany 2017; Shamshiri et al., 2018; Wang et
31 al., 2012). This may lead to an underestimation of deformation due to large temporal baseline.

32 In this manuscript, SBAS method implemented in the Stanford method for persistent scatter (referred to
33 as StaMPS-SB for simplicity) (Hooper 2008) is adopted and improved. StaMPS-SB has some advantages
34 as follows. First, it has the potential for limiting the effects of topographic errors and the decorrelation by
35 concentrating only on these interferograms with small geometric and temporal baselines (Chen et al., 2012;

1 Goel and Adam, 2012). This contributes to the reduction of phase aliasing and thereby increasing the
2 chances of successful phase unwrapping (Hooper 2008). Second, StaMPS-SB can operate on single look
3 images (Hooper 2008), by which we can avoid smoothing any change in deformation and retain the
4 deformation in the highest spatial resolution offered by the satellite. Finally, StaMPS-SB can produce the
5 temporal evolution of deformation without any prior information about its temporal evolution (Hooper et
6 al., 2007; Hooper 2008; Sousa et al., 2011). This is very useful as there is no prior knowledge about the
7 variations of deformation over the study region. However, standard StaMPS-SB adopts spectral filtering to
8 discard the non-overlapping Doppler spectrum in azimuth and to reduce the geometric decorrelation in
9 range (Hooper 2008), which leads to a coarsening of resolution and some loss of information. Thus, an
10 adaptive spatial filtering algorithm (Ferretti et al., 2011; Goel and Adam, 2011; Parizzi and Brcic, 2011) is
11 introduced in place of the spectral filtering to improve the interferometric coherence while maintaining the
12 spatial resolution. We utilize the improved StaMPS-SB to investigate the ground deformation along
13 RLSR-HZ using 124 C-band Sentinel-1 SAR images acquired from two tracks between July 2015 and
14 November 2019. Having retrieved the pattern of ground deformation, the potential causes for instability
15 along RLSR-HZ are discussed to better understand the deriving forces contributing to subsidence process.
16 Such information is the key for the safety operation and maintenance of RLSR-HZ.

17

18 **2 Study area and SAR data**

19 2.1 Study area

20 Heze region, an important part of the North China subsidence basin, is located in the lower reaches of the
21 Yellow River. This area has a relatively flat landform with altitude varying from 37 to 68 m and is covered
22 by vast areas of farmland. It is characterized by a semi-humid monsoon climate with a mean annual
23 precipitation of approximately 663 mm, which is the main recharge source of groundwater. The monsoon
24 climate makes large seasonal variations of precipitation, i.e., most of precipitation (approximately 391 mm)
25 is concentrated in the summer (Shandong Provincial Bureau of Statistics).

26 Groundwater has been a key resource for development of agriculture and industry in Heze. More than 1
27 billion tons of groundwater are exploited every year in the region by more than 110 deep wells in urban
28 area and more than 137000 wells in rural area (Xu et al., 2017). Due to the abundant extraction of
29 groundwater, the level of shallow and deep groundwater declined by more than 8 and 80 m between 1980
30 and 2013, with an average rate of 0.5m/yr and 5 m/yr respectively (Feng et al., 2015). Besides, Heze region
31 is rich in coal resources with a cumulative reserve of about 10.2 billion tons spreading over an area of 2700
32 km². Due to underground mining, an area more than 40 km² has suffered from severe subsidence.

33 RLSR-HZ, with a length of about 150 km running through Heze region from southwest to northeast
34 (shown in Fig. 1), has been under construction since December 2018 and will be operative by the end of
35 2021. Taking advantage of ballastless track, the speed reaches up to 300 Km/h. This means that a very high

1 stability of foundation is required for safety. It's crucial to accurately and continuously monitor the ground
 2 subsidence along RLSR-HZ to assess the risk.

3

4 2.2 SAR data

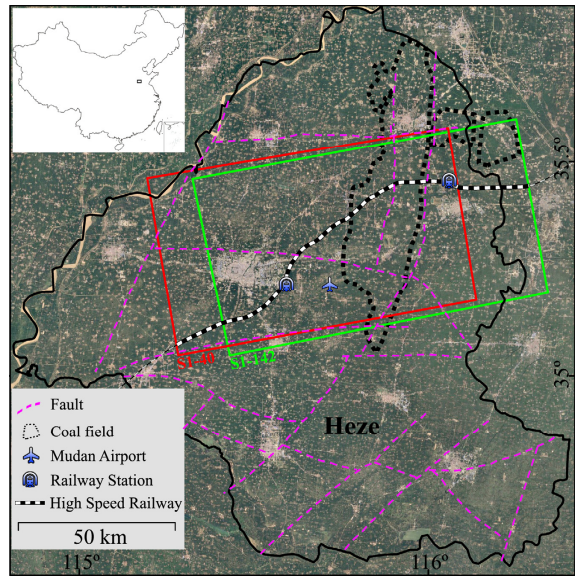
5 Our dataset includes 124 C-band Sentinel-1A SAR images in TOPS mode covering more than four years
 6 between July 2015 and November 2019. 63 of these images were collected from track 40 (referred as
 7 S1-40), and 61 from track 142 (referred as S1-142). There is no descending SAR data over this region, all
 8 these images are acquired in an ascending orbit. The ground resolution of these images is approximately 20
 9 m in azimuth and 5 m in range (Geudtner et al., 2014). The details of the Sentinel-1A datasets are
 10 summarized in Table 1. Fig. 2 shows the temporal and spatial baselines of 192 interferograms generated
 11 from S1-40 dataset and 171 interferograms generated from S1-142 dataset. It can be seen that the
 12 perpendicular baselines vary between -150 m and 150 m. External DEM data acquired from TanDEM-X
 13 with a pixel spacing of three arc second is used for removal of topographic phase component (Wessel et al.,
 14 2018) and for geometrical coregistration of TOPS data (Yague-Martinez et al., 2016).

15

Table 1. Metadata about the Sentinel-1 data used in the study.

Parameters	Description	
Dataset	Sentinel-1A	Sentinel-1A
Track	40	142
Subswath	IW3	IW1
Time span	Jul 2015–Nov 2019	Jul 2015–Nov 2019
Numer	63	61
Orbit mode	Ascending	Ascending
Incidence angle (degree)	43.8	33.8
Heading (degree)	347	347

16



17

18 Fig. 1. Study area and outline of Sentinel-1 acquisitions superimposed on Google Earth optical image (© Google Maps).

19 Black polygon represents the boundary of Heze region.

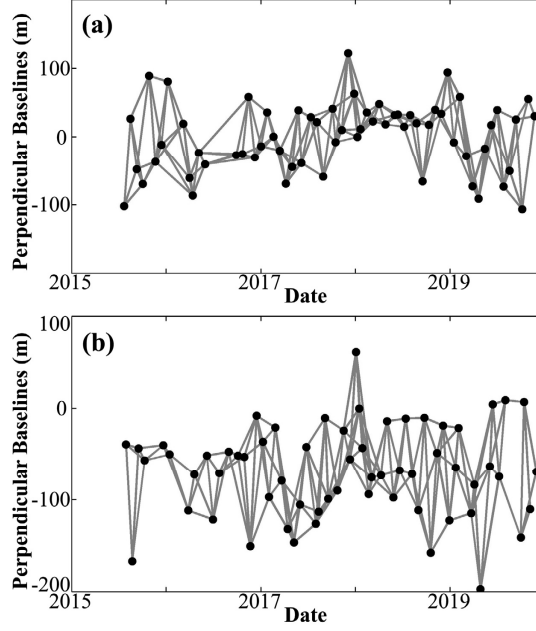


Fig. 2. Connected network of interferograms for (a) S1-40 and (b) S1-142 datasets. Black dots and grey lines denote the Sentinel-1 acquisitions and interferograms, respectively.

3 Methodology

In this study, StaMPS-SB is improved and conducted to derive the time-series displacement from multi-temporal Sentinel-1 acquisitions. Compared with single master approach (e.g, PSI), StaMPS-SB can minimize the decorrelation effects caused by long interval of SAR acquisitions and dense farmlands over this study area (Hopper 2008).

First, the S1-40 and S1-142 datasets are coregistered and resampled with respect to the reference images acquired on 8 January 2018 and 15 January 2018, respectively. The reference image should have the capability to maximize the quality index in coregistration strategy, which is dependent on the temporal and spatial baselines, the difference of Doppler centroid and thermal noise (Hopper et al., 2007). Here, we assume the thermal noise as constant for simplicity (Hopper et al., 2007).

Note that higher accuracy is required for the azimuth coregistration due to the significant Doppler frequency variation which can result in failure for traditional methods. A unique strategy combining geometric coregistration and enhanced spectral diversity (ESD) (Prats-Iraola et al., 2012) technique is used in this paper. We first perform the geometric coregistration using the precise orbit with an accuracy of 5 cm and the TanDEM-X DEM with a three arc second pixel spacing. Then, the azimuth coregistration accuracy is refined using ESD technique which exploits the differential phase in the overlap areas of consecutive bursts (Prats-Iraola et al., 2012; Yague-Martinez et al., 2016). Let Δy be the coregistration error of pixel p . According to the rationale of ESD, Δy can be estimated by (Yague-Martinez et al., 2016):

$$\hat{\Delta y} = \underset{\Delta y}{\operatorname{argmin}} \left\{ \operatorname{arg} \sum_{p \in \Omega} \exp \left(j \left(\phi_{ESD,p} - 2\pi \cdot \Delta f_{DC,p}^{covl} \cdot \frac{\Delta y}{f_{az}} \right) \right) \right\} \quad (1)$$

1 where Ω denotes the overlap area between adjacent bursts. $\phi_{ESD,p}$ is the double differential phase
 2 between adjacent bursts. $\Delta f_{DC,p}^{covl}$ and f_{az} are the Doppler centroid frequency difference and the azimuth
 3 sampling frequency, respectively.

4 After that, all the images (i.e., the resampled images and the reference image) are recombined with each
 5 other to generate interferograms as long as the geometric and temporal baselines are less than a predefined
 6 threshold. A small orbital separation (i.e., 150 m) is specified as the geometric baseline threshold in order to
 7 restrain the effect of spatial decorrelation noise and topographic errors. Meanwhile, a short interval (i.e., 84
 8 days) is specified as the temporal baseline threshold in order to restrain the effect of temporal decorrelation
 9 noise and accumulative deformation on wrapped phase. Then, all the interferograms are inspected to
 10 distinguish the noisy interferograms which will be excluded from the network. In addition, the temporal
 11 intervals of interferograms are not very uniform. Some gaps are being more than 84 days, which results in a
 12 disconnected network for the auto-generated interferograms. Therefore, some interferograms with high
 13 coherence are manually appended to the original stacks to form a connected network which is essential for
 14 StaMPS-SB. Finally, two connected networks containing 192 interferograms for S1-40 and 171
 15 interferograms for S1-142 are generated, respectively (shown in Fig. 2). In these networks, each image is
 16 connected to at least two other images, by which the temporal sampling rate is increased by an average
 17 factor of 2.9. Taking advantage of the adequate interferograms, the model parameters such as deformation,
 18 topographic errors and atmospheric artifacts can be estimated more accurately comparing with single
 19 master approach.

20 Generally, multi-looking (Berardino et al., 2002) and spectral filtering (Hooper 2008) are the common
 21 approaches to improving interferometric coherence and reducing noise. Standard StaMPS-SB adopts
 22 spectral filtering to discard the non-overlapping Doppler spectrum in azimuth and to reduce the geometric
 23 decorrelation in range. However, the spectral filtering operation leads to a coarsening of resolution (Hooper
 24 2008), which therefore may cause some loss of deformation information. In fact, the differences in Doppler
 25 frequency of Sentinel-1 data are only a few Hz (Yague-Martinez et al., 2016) and the common Doppler
 26 bandwidth is more than 95% in most cases. Additionally, the range bandwidth is larger than 40 MHz and
 27 almost all of the geometric baselines are shorter than 150 m. As a result no spectral filtering is applied to
 28 avoid coarsening the resolution. In contrast, an adaptive spatial filtering algorithm (Ferretti et al., 2011;
 29 Goel and Adam, 2011; Parizzi and Bricc, 2011) is introduced and implemented to improve the
 30 interferometric phase and coherence while preserving the image details. The key element of adaptive
 31 spatial filtering is the identification of statistically homogenous pixels (SHP). Let A_p be the amplitudes of
 32 pixel p :

$$33 \quad A_p = [A_1(p), A_2(p), \dots, A_M(p)] \quad (2)$$

1 where M is the number of SAR images. Let A_q be the amplitudes of pixel q located in the estimation
 2 window centered on p , and $A_q = [A_1(q), A_2(q), \dots, A_M(q)]$. We can use statistical hypothesis testing to
 3 evaluate whether p and q are SHP (Samiei-Esfahany 2017):

$$4 \quad H_0 : F_{A_p} = F_{A_q}, \quad H_1 : F_{A_p} \neq F_{A_q} \quad (3)$$

5 where F_{A_p} and F_{A_q} are the cumulative distribution function of amplitudes of p and q , respectively.

6 In this paper, the Kolmogorov-Smirnov (KS) test is used to identify the SHP in a rectangular window with
 7 a dimensions of 19×13 (azimuth \times range). The adaptive spatial filtering will be carried only if the number
 8 of SHP is greater than 18 by which to preserve PS information.

9 StaMPS-SB selects coherent targets based on the phase characteristics (Hooper 2008),

$$10 \quad \gamma_x = \frac{1}{N} \left| \sum_{i=1}^N \exp \left\{ \sqrt{-1} (\varphi_{x,i} - \tilde{\varphi}_{x,i} - \Delta\phi_{\theta,x,i}^{\mu}) \right\} \right| \quad (4)$$

11 where $\varphi_{x,i}$ is the wrapped phase of candidate pixel x in the i th filtered interferogram. $\tilde{\varphi}_{x,i}$ is the
 12 estimated spatially correlated terms. $\Delta\phi_{\theta,x,i}^{\mu}$ is the spatially uncorrelated terms due to look angler error
 13 which is correlated with the perpendicular baseline. N is the number of interferograms. Candidate pixels
 14 are firstly selected using the amplitude difference dispersion (a threshold of 0.6 is adopted). Then, these
 15 candidates will be filtered in small patches, such as $50 \text{ m} \times 50 \text{ m}$, to estimate $\tilde{\varphi}_{x,i}$. Finally, coherent targets
 16 will be determined through an iterative procedure estimating the noise (γ_x) of each candidate by
 17 implementing the inversion of $\Delta\phi_{\theta,x,i}^{\mu}$ as a search of parameter space. Further details on the selection
 18 method can be found in Hooper et al., (2007) and Hooper (2008).

19 Once the coherent targets have been determined, the differential interferometric phase of each coherent
 20 target is corrected using the estimated spatially uncorrelated terms (i.e. $\Delta\phi_{\theta,x,i}^{\mu}$) in Eq. (4). After removal of
 21 $\Delta\phi_{\theta,x,i}^{\mu}$, the residual phase mainly consists of ground deformation, atmospheric artifacts and orbit error, and
 22 then can be unwrapped using the three-dimensional (3-D) algorithm (Hooper and Zebker, 2007). Firstly, the
 23 difference phase between neighboring coherent targets is preliminarily unwrapped in time under the
 24 Nyquist assumption (Hooper 2010). A priori probability density function (PDF) can be built in each
 25 interferogram based on the unwrapped difference phase in time dimension. These PDFs are then used to
 26 search for the optimization routines of unwrapping in space to achieve the final unwrapped results (Hooper
 27 2010). Subsequently, the time series deformation of each coherent target can be extracted by temporal and
 28 spatial filtering based on the characteristics of each phase terms.

Note that InSAR is a relative measure to reference point. In order to derive the absolute results, the deformation of reference point should be known. However, there is no available prior information about the deformation in Heze region. In contrast to the standard procedure of StaMPS-SB that only selects one reference area, we identify some possible areas not affected by deformation based on the differential phase in time series. By using multiple reference areas, we can minimize the error of the InSAR-derived deformation due to misplaced of single area (Fiaschiet al., 2017).

4 Results

4.1 Cross validation of the displacement

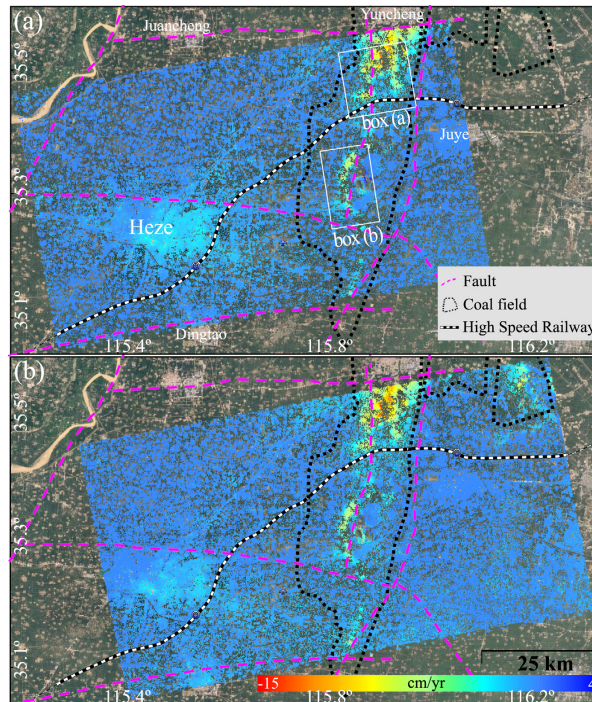


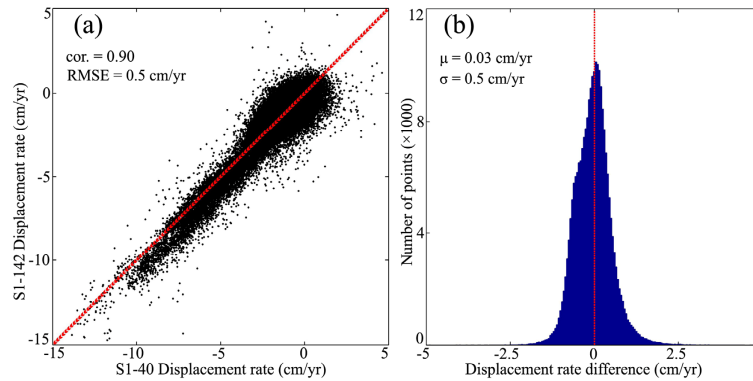
Fig. 3. The average rates of land displacement results from (a) S1-40 and (b) S1-142, superimposed on Google Earth optical image (© Google Maps). The two white boxes (indicated by a and b) indicate the locations of subsidence area related to underground mining shown in Fig. 9-10 and analyze in Sec. 5.2.

Fig. 3 shows the displacement rates derived from S1-40 and S1-142. The negative displacement indicates that the ground was subjected to subsidence during this period.

As no *in-situ* data is publicly available, we assess the consistency and precision of InSAR results by a cross comparison (shown in Fig. 4) of the displacement rates derived from the S1-40 and S1-142. Although the sensor's physical parameters are the same, the location of two sets of measurement points (MPs, consisting of PS and DS pixels) is slightly different due to the different geometric parameters. In order to identify the common MPs, both results from S1-40 and S1-142 are resampled to a grid with a spacing of 50 m. The displacement rates are averaged if multiple MPs are located in the same grid. Besides, the displacements are converted to vertical direction assuming that the horizontal displacements are negligible. 232984 common MPs are finally identified after the above procedure. Based on these common MPs, we

1 estimate the Pearson correlation of the two measurements getting a correlation of 0.9 (shown in Fig. 4a).
2 We also calculate the root mean square error (RMSE) of the two InSAR results, getting a RMSE of 0.5
3 cm/yr. The low RMSE and high correlation demonstrates the consistency of the InSAR results.

4 The variation in the difference between the two measurements illustrated in Fig. 4b provides an
5 estimation about the precision of S1-40 and S1-142 InSAR results. We calculate the mean (μ) and standard
6 deviation (σ) of the difference of displacement rates, getting values of 0.03 cm/yr and 0.5 cm/yr,
7 respectively. Therefore, we conclude that the two InSAR results agree well with each other and the
8 precision (i.e., $1-\sigma$ uncertainty) of the two measurements is about 0.5 cm/yr.

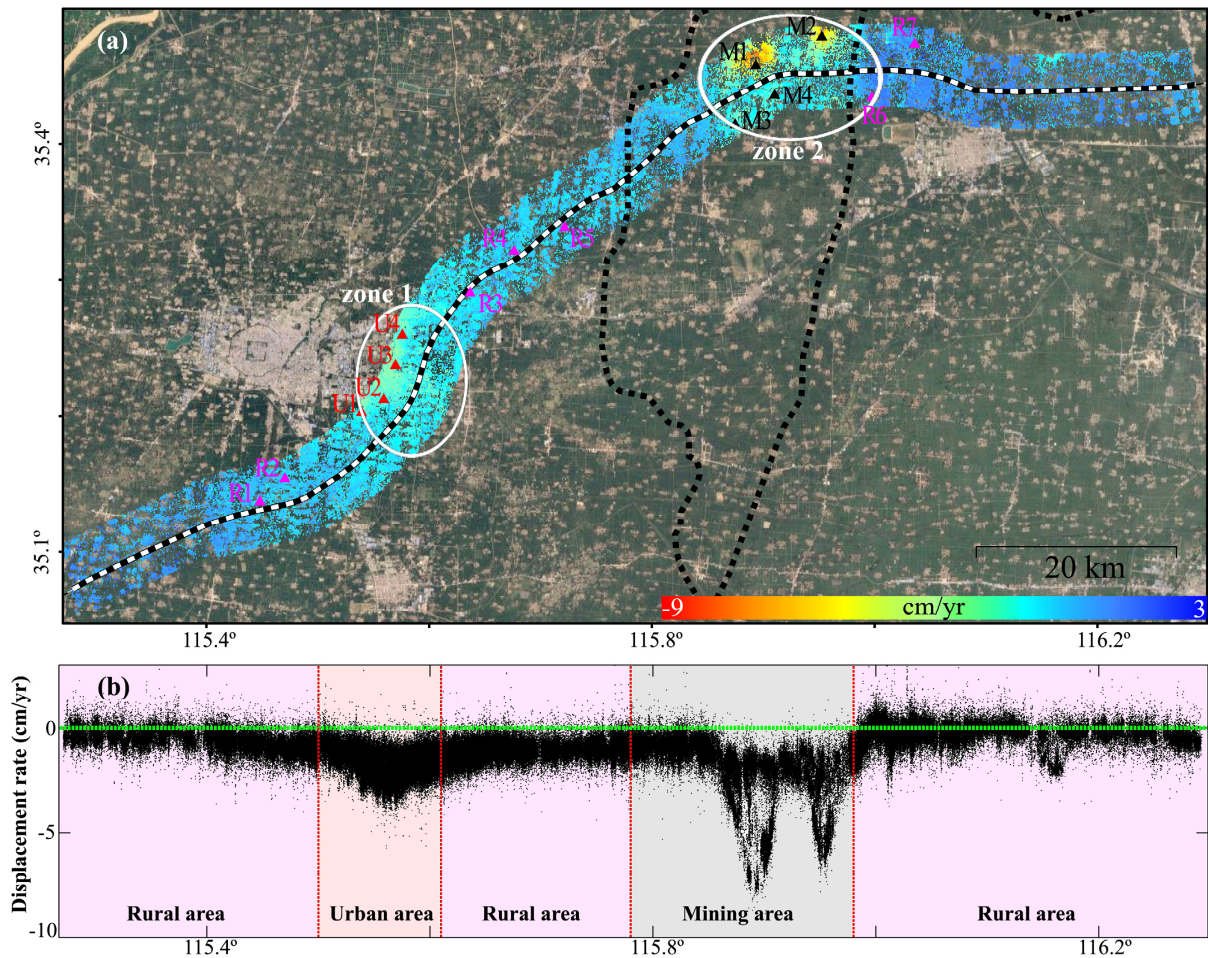


9
10 Fig. 4. The cross-validation of InSAR results from S1-40 and S1-142. The correlation and the difference between the two
11 measurements are shown in (a) and (b), respectively.
12

13 4.2 Land displacement along the RLSR-HZ

14 The displacement rates within a radius of 3 km along the RLSR-HZ are illustrated in Fig. 5. The total
15 numbers of MPs from the two sets of data are up to 312702 and 261397, resulting in an average density of
16 approximately 473 and 375 MPs/km², respectively. With the advantage of dense MPs, ground deformation
17 along the RLSR-HZ can be represented in detail compared to conventional methods. Note that the spatial
18 density of MPs is not homogeneous due to different ground scatterer characteristics. The MPs are evenly
19 distributed in urban area because of dense hard objects while sparsely distributed in rural area due to the
20 vegetation cover. To increase the density of MPs, the two measurements derived from S1-40 and S1-142
21 datasets are both shown in Fig. 5. Thus, there are more MPs in the overlapping area.

22 Fig.5a shows the displacement rates along the designed RLSR-HZ. It can be seen that the RLSR-HZ runs
23 through two subsidence zones (two black ellipses in Fig.5a), one of which (zone 1) is located in the east of
24 the Heze city and another one (zone 2) in the mining area. In zone 1, the displacement rates range from -4
25 cm/yr to -1 cm/yr. The subsidence pattern is smooth and homogeneous in space. A length of approximately
26 20 km of RLSR-HZ will be affected by the subsidence. In contrast, a stronger subsidence is observed in
27 zone 2, and a length of approximately 15 km of RLSR-HZ will be affected. The displacement rates detected
28 by InSAR range from -8 cm/yr to -2 cm/yr.



1
2 Fig. 5. (a) The spatial distribution and (b) the profile of average displacement rates along RLSR-HZ. Both the results from
3 S1-40 and S1-142 are shown, which leads to a denser MPs in the overlapping area. Two ellipses show the major subsidence
4 area. The triangles (i.e., pink triangles named as R1-R7, red triangles named as U1-U4 and black triangle named as M1-M4)
5 delineate the displacement features in rural area, urban area and mining area discussed in detail in Fig. 6-8, respectively. The
6 base map in (a) is from Google Earth optical image (© Google Maps).

7 To make further investigation on the ongoing settlement, we estimate the displacement profile along the
8 RLSR-HZ and show the results in Fig.5b. It can be seen that the deformation pattern is not homogenous
9 along the RLSR-HZ. The ground experiences strongest subsidence in the underground mining area,
10 followed by the urban area. We also observe slightly deformation in rural area, where the displacement
11 rates range between -2 cm/yr to 1 cm/yr. However, another subsidence area with the maximum rates up to
12 -3 cm/yr appears near the 116.16°. This area is offset from the coalfield by 3.5 km, so the subsidence
13 phenomenon there might be related to the underground mining.

14 4.3 Heze Mudan Airport

15 Another remarkable subsidence feature is a localized area around the Heze Mudan Airport (HMA)
16 (shown in Fig. 3). HMA has been under construction since 2017 and will open and serve Shandong with
17 domestic flights in 2020 according to the schedule. InSAR deformation maps (Fig. 3) show a subsidence
18 feature near the airport with a maximal displacement rate of approximately -3 cm/yr. The ancillary facilities
19

1 of the airport, such as the runway and terminal buildings, are also affected by nonuniform subsidence
2 ranging from -3 cm/yr to -0.5 cm/yr.

4 **5 Discussion**

5 Several possible causes, including natural factors and anthropogenic activities, could be related to the
6 deformation patterns observed in Heze. Tectonic movement and underground caves can cause ground
7 deformation. However, the high displacement rates, which exceed 5 cm/yr at many locations, are not in
8 agreement with the tectonic movement rates which are estimated to be less than 0.5 cm/yr (Guo et al.,
9 2019). In addition, there are no known underground caves associated with sinkholes or karst landforms in
10 this region. In contrast, according to close inspections of the subsidence area and considering the
11 underground mining coupled with the decreasing hydraulic heads in this region, we infer that this
12 deformation is mainly caused by extensive extraction of groundwater and coal mine. This will be
13 elaborated more in the following.

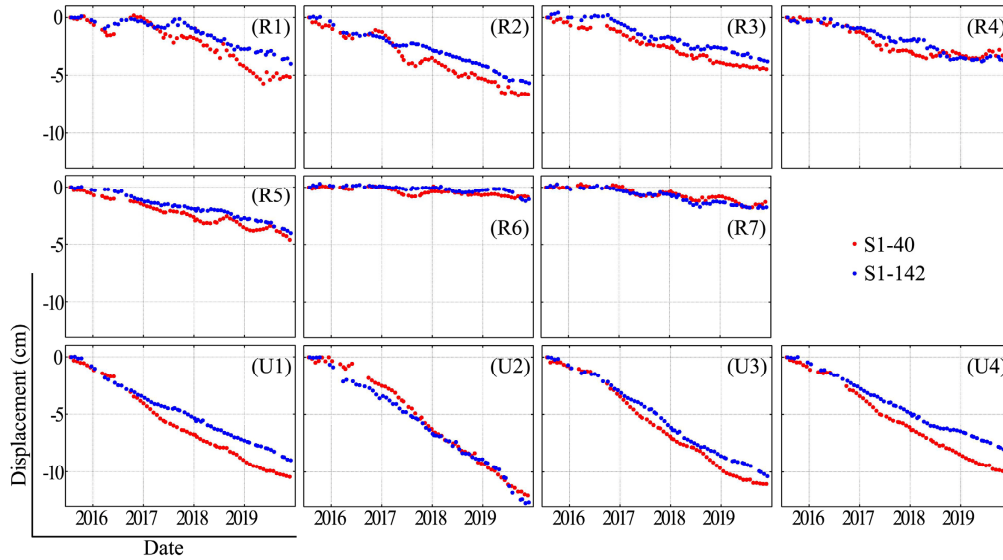
15 5.1 Correlation between ground deformation and groundwater withdraw

16 Groundwater has been exploited for agricultural irrigation, industrial and residential use in Heze region
17 since the early 1970s. Long-term exploitation of groundwater brings about a compaction of the fine clay
18 layer, and finally results in the ground subsidence. Previous researches indicate that the excessive
19 groundwater withdrawal is one of the main reasons for ground deformation in this area (Hu et al., 2004;
20 Guo et al., 2019; Xue et al., 2005).

21 To better understand the ground motion, the time series displacements of MPs located within a 50 m
22 radius around 11 points (marked by red and pink triangles in Fig .5) are shown in Fig .6. It can be seen that
23 most of these locations suffer from ground subsidence in the period from July 2015 to November 2019. It
24 suggests that the groundwater is still excessively exploited and the groundwater recharge is insufficient to
25 supply the exploitation. Fig. 7a and 7b show that both the shallow and deep groundwater level declined in
26 recent years. Xu et al., (2017) pointed out that more than 1 billion tons of groundwater is over-extracted
27 annually by more than 137000 wells in Heze region.

28 Besides, Fig .6 shows that the behavior of the time series displacement significantly differs in rural area
29 and urban area. Comparing with rural area, the ground experiences more serious subsidence in urban area.
30 One reason for the large settlement in urban area is that the deep groundwater (over 200 m depth) is
31 massively extracted to meet the industrial need, except for shallow groundwater to domestic use. It can be
32 seen from Fig. 7a and 7b that the shallow groundwater level declined 0.5 m from July 2016 to July 2017,
33 while the deep groundwater level declined approximately 6 m from July 2015 to October 2017.
34 Approximately 0.16 billion tons of groundwater is over-extracted annually by more than 110 deep wells in
35 urban area of Heze (Xu et al., 2017; Shandong Provincial Bureau of Statistics). The level of deep

1 groundwater declined by more than 100 m between 1980 and 2018 (Feng et al., 2015; Yue 2020). However,
 2 many thick clay layers over the confined aquifer restrict the flow for aquifer recharging from precipitation
 3 in vertical direction. Meanwhile, the recharge rates of deep groundwater in the horizontal direction, i.e.,
 4 running off along the topography from west to east, is very slow (Qiao and Lin 2006; Zhang 2013).



5
 6 Fig. 6. Time series displacement of MPs located in rural area (R1-R7) and urban area (U1-U4) shown in Fig. 5.

7 As the aquifer's detailed information is not public, we cannot obtain enough information to investigate
 8 the detailed relationship between the subsidence and the groundwater level. However, the precipitation is
 9 the main recharge source of shallow groundwater (accounting for 85% of the total supply) in this region
 10 and directly determines the level of shallow groundwater (Jia 2015; Ma and Feng, 2014; Yu et al., 2001).
 11 Therefore, we switch to investigate the relationship between the subsidence and the precipitation.

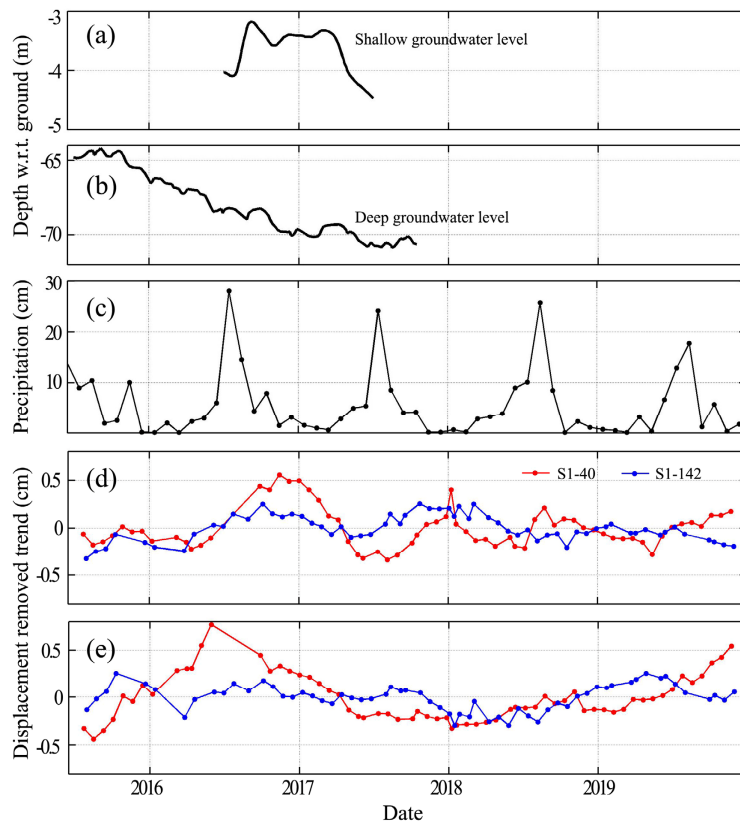
12 The precipitation from July 2015 to December 2019 is presented in Fig. 7c. We can infer the variation of
 13 shallow groundwater according to the precipitation. Generally, the precipitation, exploitation and
 14 evaporation of groundwater are little from January to February in Heze region. During this period, the
 15 groundwater level is relatively stable and rises slowly until the beginning of March. In addition, the freeze
 16 of water contained in the soil due to the low temperature, can also increase the groundwater volume and
 17 results in an inflation. From March to June, the little precipitation and massive groundwater extraction to
 18 irrigate crops result in a continuous decline of groundwater level until the beginning of the rainy season.
 19 The water level rebounds from July to September due to lots of precipitation (seen Fig. 7a), and maintains a
 20 relatively stable rate due to the decreasing of extraction from October to December (Jia 2015).

21 The average time series displacement of all points located in rural area, after removing its trend, is used
 22 as an average representation of the variations of rural area and shown in Fig. 7d, while the average
 23 variations of urban area is shown in Fig. 7e.

24 The deviation in rural area (Fig. 7d) indicates that the ground fluctuates by approximately ± 0.5 cm with a
 25 significant seasonal variation. The latter may be related to the seasonal variation of aquifer water level

1 which is determined by the seasonal precipitation (seen Fig. 7a and 7c). In addition, as shown in Fig. 7d,
 2 the variations of displacement in rural areas have a significant correlation with precipitation with a time lag
 3 of approximately two months. According to the Fig.7a, 7c and 7d, we may hypothesize that the ground
 4 subsidence is caused by both the hydraulic head change and the seasonal groundwater variations. Moreover,
 5 the time lag is induced by the groundwater level increases arising from the seasonal precipitation.

6 In contrast, Fig. 7e shows that there is no straightforward relationship between the precipitation and the
 7 variations of displacement in urban area. It may be due to the extraction of deep rather than shallow
 8 groundwater as the deep groundwater is difficult to recharge due to the complicated geological conditions
 9 in this region (Qiao and Lin 2006; Zhang 2013). Zhang et al., (2018) found that the subsidence has a
 10 significant correlation (up to 0.96) with the declining of deep groundwater level in another city near Heze.



11
 12 Fig. 7.(a) Shallow and (b) deep ground level with respect to the ground. (c) Monthly precipitation for the Heze region during
 13 July 2015 and December 2019. After removing the linear trend, the average of residual time series displacement of (d) R1-R7
 14 in rural area and (e) U1-U4 in urban area.

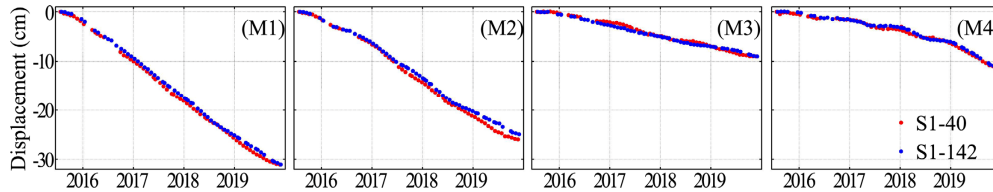
15

16 5.2 Correlation between ground deformation and underground mining

17 Fig .8 shows the time series displacements at four locations (M1~M4 in Fig. 5) above coalfield. Fig. 5
 18 and Fig. 8 show that the cumulative subsidence above coal does not exceed 50 cm for more than four years.
 19 In addition, Fig. 8 reveals a significant linear displacement trend. In fact, the mining-induced subsidence is
 20 generally nonlinear with high rates, which can reach up to several meters in a short time (e.g. several
 21 months). These characteristics indicate that the subsidence near M1~M4 locations may not be directly

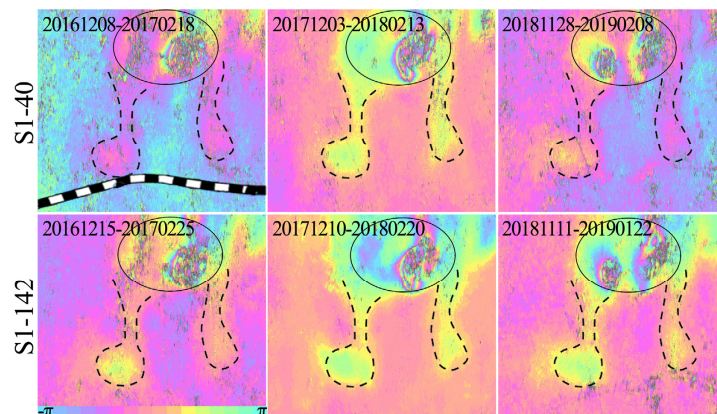
1 induced by underground mining.

2 Note that the underground mining inevitably produces many fracture fields which may be interconnected
3 with the faults, forming a vast interconnected network. The groundwater flows into the working planes
4 through fractures and is drained out (Rapantova et al., 2007; Xu et al., 2018), which finally results in the
5 ground subsidence. Also, underground mining may destroy the stability of faults and induce faults slipping
6 (Islam and Shinjo, 2009; Wang et al., 2016; Zhang et al., 2018), which can also lead to ground subsidence.



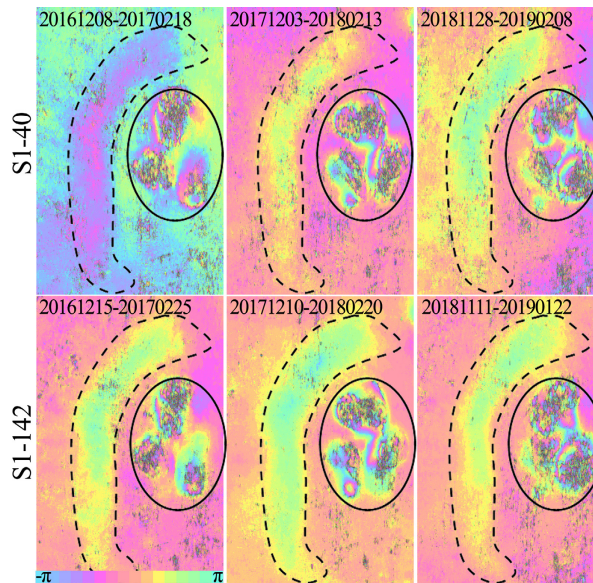
7
8 Fig. 8. Time series displacement of MPs located in mining area (M1-M4) shown in Fig. 5.

9 Fig. 9 shows six interferograms of box (a) in Fig. 3a. We observe that there are several active subsidence
10 areas, represented by dense fringes (ellipses in Fig. 9), located in 5~8 km north of M1 and M2 locations.
11 The loss of signal in the central of these subsidence areas is probably due to the displacement, being too
12 large to be detected by MT-InSAR with the C-band Sentinel-1 data. This conforms to the mining-induced
13 displacement field which presents a bowl-shaped subsidence pattern, as observed in other studies (He et al.,
14 1994; Litwiniszyn 1956; Zhu et al., 2020). The dense fringes, i.e., strong deformation, suggests active
15 underground mining just below this subsidence basin (referred to as primary subsidence basin and denoted
16 by ellipses in Fig. 9). In contrast, all the six interferograms and the corresponding displacement rates shown
17 in Fig. 3 reveal a relatively slight subsidence near M1 and M2 locations (referred as secondary subsidence
18 basin) in comparison to the primary subsidence basin. Close inspections of fringes distribution in Fig. 9
19 show that the ground deformation seems to progress to M1 and M2 area along with two ‘galleries’ (dashed
20 line in Fig. 9). A plausible explanation of this deformation near M1 and M2 locations could be the
21 groundwater outflow to working panels and its drainage, which finally triggers the ground subsidence.



22
23 Fig. 9 .Example of interferograms produced from S1-40 and S1-142 of box (a) in Fig. 3. The ellipses show the primary
24 subsidence area induced by underground mining. One color fringe stands for approximately 2.8 cm displacement in the LOS.
25 The dashed lines show the secondary subsidence area caused by complicated factors, e.g, groundwater drain out and/or fault
26 activation due to underground mining.

1 In addition, a similar phenomenon is observed in an area (box (b) in Fig.3a) 5-11 km south of RLSR-HZ.
 2 Fig. 10 shows six interferograms of this area. In the right (ellipses in Fig. 10), the dense fringes in this
 3 primary subsidence area imply active underground mining. However, an arc-shape secondary subsidence
 4 area (dashed line in Fig. 11) with a length of about 14 km is observed within 3 km to the left of the primary
 5 subsidence area. The arc-shape subsidence does not agree with the law of the ground movement induced by
 6 underground mining. Fig.3 shows the arc-shape subsidence is consistent with the fault, which implies that
 7 the underground mining causes the fault activation and results in ground deformation. Unfortunately, it is
 8 difficult to investigate the interactions among the underground mining, fault activation and ground
 9 deformation, since we do not have detailed information, such as the distribution of unknown faults and
 10 abandoned mines, the relative position of the faults and mining sites. Nevertheless, the concomitant ground
 11 deformation (i.e., secondary subsidence basin) induced by underground mining suggests that it must be
 12 very careful to extract coal, especially when there are widespread faults.



13
 14 Fig. 10 . Example of interferograms produced from S1-40 and S1-142 of box (b) in Fig. 3. The ellipses show the primary
 15 subsidence area induced by underground mining. One color fringe stands for approximately 2.8 cm displacement in the LOS.
 16 The dashed lines show the secondary subsidence area caused by complicated factors, e.g, groundwater drain out and/or fault
 17 activation due to underground mining.

18

19 **6 Conclusion**

20 This study investigates the time series displacement over Heze region in 2015-2019 using MT-InSAR
 21 based on two sets of Sentinel-1A datasets. The two independent MT-InSAR results agree well with each
 22 other with $1-\sigma$ uncertainty of approximately ± 0.5 cm/yr. Focusing on the ground displacement along
 23 RLSR-HZ, we find that there are two main ground subsidence zones:

- 24 - One subsidence zone is located in the east of Heze city ($115.5^{\circ}\text{E} \sim 115.6^{\circ}\text{E}$) with displacement rates
 25 ranging from -4 cm/yr to -1 cm/yr. A length of approximately 20 km of RLSR-HZ will be affected
 26 by this subsidence.

1 - One subsidence zone is located in the coalfield (115.8°E ~ 116.0°E) with displacement rates ranging
2 from -8 cm/yr to -2 cm/yr. A length of approximately 15 km of RLSR-HZ will be affected by this
3 subsidence.

4 Considering the previous investigation coupled with information of human activities, we conclude that
5 the subsidence is mainly caused by extraction of groundwater and underground mining:

6 - By combining the known previous investigations and the monthly precipitation, we find two patterns
7 of subsidence: a long-term subsidence due to the extraction of deep groundwater mainly in the urban
8 area, and short-term variations related to the seasonal precipitation in the rural area.

9 - Underground mining is another cause of ground subsidence, which can reach up to several meters.
10 However, we found an interesting phenomenon of a secondary subsidence basin further away (about
11 3-7 km) from the primary subsidence basin (Fig. 9 and 10). Considering the known faults and the
12 unknown mining-induced fracture fields, we infer that the secondary subsidence is very probably
13 caused by the groundwater outflow and fault instability due to mining, rather than being directly
14 caused by mining. It will be interesting to further investigate the cause of secondary subsidence
15 when more data become available.

16 It is very difficult to restore the surface elevation and the foundation stability after extracting deep
17 groundwater and coal mine. The ongoing subsidence will severely damage the infrastructures of RLSR-HZ,
18 particularly when the RLSR-HZ will be operational by the end of 2021. Effective management in
19 groundwater and coal mine is an urgent need to implement. Hence, it is very meaningful to continue the
20 monitoring ground deformation along RLSR-HZ using multiple SAR data.

21
22 **Data availability.** Sentinel-1A/B data are available at <https://scihub.copernicus.eu/>. TanDEM-X are freely downloaded from
23 <https://sso.eoc.dlr.de/eoc/auth/login?service=https://download.geoservice.dlr.de/TDM90/files/>. The monthly precipitation are
24 available at <http://data.cma.cn/>. The information about the annual exploitation of groundwater is provided by Shandong
25 Provincial Bureau of Statistics from <http://www.stats-sd.gov.cn/col/col6279/index.html?uid=29225&pageNum=1>.

26
27 **Author contributions.** CZ initiated the study and wrote the manuscript. WW provided python scripts for analysis. CZ and
28 MM analyzed the data. MM, LZ, ZJ and SL provided advice and reviewed the manuscript.

29
30 **Competing interests.** The authors declare that they have no conflict of interest.

31
32 **Acknowledgements.** Thanks go to the StaMPS software that can be downloaded from
33 <http://homepages.see.leeds.ac.uk/~earahoo/stamps/index.html>. The authors would also like to thank the editor Antonio
34 Montuori, reviewers Darvishi Mehdi and Argyrakis Panagiotis, and the anonymous reviewers for their careful work and
35 insightful suggestions.

36

1 **Financial support.** This research was supported by the National Natural Science Foundation of China (41901373 and
2 41877283), the Natural Science Foundation of Hunan Province (2019JJ50190). The authors would also like to thank the
3 reviewers for their careful work. Thanks go to the StaMPS software that can be downloaded from
4 <http://homepages.see.leeds.ac.uk/~earahoo/stamps/index.html>.

5

6 **References**

- 7 Vervoort, A.: Surface movement above an underground coal longwall mine after closure, *Natural Hazards and Earth System*
8 *Sciences*, 16, 2107–2121, <https://doi.org/10.1016/j.ijmst.2017.03.007>, 2016.
- 9 Berardino, P., Fornaro, G., Lanari, R., and Sansosti, E.: A New Algorithm for Surface Deformation Monitoring Based on
10 Small Baseline Differential SAR Interferograms, *IEEE Transactions on Geoscience and Remote Sensing*, 40, 2375–2383,
11 <https://doi.org/10.1109/TGRS.2002.803792>, 2002.
- 12 Bamler, R., and Hartl, P.: Synthetic aperture radar interferometry, *Inverse Problems*, 14, R1–R54,
13 <https://doi.org/10.1088/0266-5611/14/4/001>, 1998.
- 14 Chen, F. L., Lin, H., Li, Z., Chen, Q., and Zhou, J. M.: Interaction between permafrost and infrastructure along the
15 Qinghai-Tibet Railway detected via jointly analysis of C- and L-band small baseline SAR interferometry, *Remote Sensing*
16 *of Environment*, 123, 532–540, <https://doi.org/10.1016/j.rse.2012.04.020>, 2012.
- 17 Cui, Z. D.: *Land Subsidence Induced by the Engineering-Environmental Effect*, Springer Singapore, Singapore, 2018.
- 18 Du, Z. Y., Ge, L. L., Ng, H. M. , and Li, X. J.: Investigation on mining subsidence over Appin-West Cliff colliery using
19 time-series SAR interferometry, *International Journal of Remote Sensing*, 39, 1528–1547,
20 <https://doi.org/10.1080/01431161.2017.1407501>, 2018.
- 21 Feng, C. C., Ma, X. F., and Huang, W. F.: Analysis on land subsidence survey and trend in Heze city, in: 13th Geoscience and
22 Technology Forum of East China, Nanchang, China, 1 November 2015, 383–387, 2015.
- 23 Ferretti, A., Fumagalli, A., Novali, F., Prati, C., Rucci, A., and Rucci, A.: A new algorithm for processing interferometric
24 data-stacks: squeeSAR, *IEEE Transactions on Geoscience and Remote Sensing*, 49, 3460–3470, <https://doi.org/10.1109/TGRS.2011.2124465>, 2011.
- 25 Ferretti, A., Prati, C., and Rocca, F.: Non-linear Subsidence Rate Estimation Using Permanent Scatterers in Differential SAR
26 Interferometry, *IEEE Transactions on Geoscience and Remote Sensing*, 38, 2202–2212, <https://doi.org/10.1109/36.868878>,
27 2000.
- 28 Ferretti, A., Prati, C., and Rocca, F.: Permanent Scatterers in SAR Interferometry, *IEEE Transactions on Geoscience and*
29 *Remote Sensing*, 39, 8–20, <https://doi.org/10.1109/36.898661>, 2001.
- 30 Fiaschi, S., Closson, D., Karaki, N. A., Pasquali, P., Riccardi, P., and Floris, M.: The complex karst dynamics of the Lisan
31 Peninsula revealed by 25 years of DInSAR observations. Dead Sea, Jordan, *ISPRS Journal of Photogrammetry and*
32 *Remote Sensing*, 130, 358–369, <https://doi.org/10.1016/j.isprsjprs.2017.06.008>, 2017.
- 33 Gabriel, A. K., Goldstein, R. M., and Zebker, H. A.: Mapping Small Elevation Changes over Large Areas: Differential Radar
34 Interferometry, *Journal of Geophysical Research*, 94, 9183–9191, <https://doi.org/10.1029/JB094iB07p09183>, 1989.
- 35 Geudtner, D., Torres, R., Snoeij, P., Davidson, M., and Rommen, B.: Sentinel-1 System capabilities and applications, in:
36 Proceedings of IEEE International Conference on Geoscience and Remote Sensing Symposium, IGARSS 2014, Quebec,
37 Canada, 13–18 July 2014, 1457–1460, 2014.
- 38 Goel, K., and Adam, N.: High resolution differential interferometric stacking via adaptive spatial phase filtering, in:
39 Proceedings of IEEE International Conference on Geoscience and Remote Sensing Symposium, IGARSS 2011, Vancouver,
40 Canada, 24–29 July 2011, 1341–1344, 2011.
- 41 Goel, K., and Adam, N.: An advanced algorithm for deformation estimation in non-urban areas, *ISPRS Journal of*
42 *Photogrammetry and Remote Sensing*, 73, 100–110, <https://doi.org/10.1016/j.isprsjprs.2012.06.001>, 2012.
- 43

1 Goodman, J. W.: Some fundamental properties of speckle, *Journal of the Optical Society of America*, 66, 1145–1150,
2 <https://doi.org/10.1364/JOSA.66.001145>, 1976.

3 Guo, C. X., Nie, J. L., Tian, J., Wang, W. L., Cheng, C. L., Wang, B., Yin, H. F., and Zhang, H. P.: Vertical ground
4 displacements in the Shandong Province derived from long-term GNSS and leveling surveying, *Advances in Space*
5 *Research*, 64, 1388–1397, <https://doi.org/10.1016/j.asr.2019.06.035>, 2019.

6 Haghighi, M. H., and Motagh, M.: Ground surface response to continuous compaction of aquifer system in Tehran, Iran:
7 Results from a long-term multi-sensor InSAR analysis, *Remote Sensing of Environment*, 221, 534–550,
8 <https://doi.org/10.1016/j.rse.2018.11.003>, 2019.

9 He, G. Q., Yang, L., Lin, G. D., Jia, F. C., and Hong, D.: *Mining Subsidence Engineering*, Press China Univ. Mining Technol,
10 Xuzhou, China, 1994.

11 Hooper, A.: A Multi-Temporal InSAR Method Incorporating Both Persistent Scatterer and Small Baseline Approaches,
12 *Geophysical Research Letters*, 35, L16302, <https://doi.org/10.1029/2008GL034654>, 2008.

13 Hooper, A.: A statistical-cost approach to unwrapping the phase of InSAR time series, in: *Proceedings of the International*
14 *Workshop on ERS SAR Interferometry*, Frascati, Italy, 30 November – 4 December, 1–4, 2010.

15 Hooper, A., and Zebker, H.: Phase unwrapping in three dimensions with application to InSAR time series, *Journal of Optical*
16 *Society of America*, 24, 2737–2747, <https://doi.org/10.1364/JOSAA.24.002737>, 2007.

17 Hooper, A., Segall, P., and Zebker, H.: Persistent Scatterer Interferometric Synthetic Aperture Radar for Crustal Deformation
18 Analysis, with Application to Volcán Alcedo, Galápagos, *Journal of Geophysical Research*, 112, B07407,
19 <https://doi.org/10.1029/2006JB004763>, 2007.

20 Hu, R. L., Yue, Z. Q., Wang, L. C., and Wang, S. J.: Review on current status and challenging issues of land subsidence in
21 China, *Engineering Geology*, 76, 65–77, 2004.

22 Hung, W. C., Hwang, C., Chen, Y. A., Chang, C. P., Yen, J. Y., Hooper, A., and Yang, C. Y.: Surface deformation from
23 persistent scattererssar interferometry and fusion with leveling data: a case study over the choushui river alluvial fan,
24 Taiwan, *Remote Sensing of Environment*, 115, 957–967, <https://doi.org/10.1016/j.rse.2010.11.007>, 2011.

25 Islam, M. R., and Shinjo, R.: Mining-induced fault reactivation associated with the main conveyor belt roadway and safety of
26 the Barapukuria Coal Mine in Bangladesh: Constraints from BEM simulations, *International Journal of Coal Geology*, 79,
27 115–130, <https://doi.org/10.1016/j.coal.2009.06.007>, 2009.

28 Jia, P. Y.: Investigation and evaluation of groundwater environment in Heze City, *Zhihuai*, (1), 83–84, 2015.

29 Kampes, B.: *Radar Interferometry: Persistent Scatterer Technique*, Springer Netherlands, Netherlands, 2006.

30 Litwiniyszyn, J.: Application of the equation of stochastic processes to mechanics of loose bodies, *Archives Mechanics*, 8,
31 393–411, 1956.

32 Ma, L., and Feng, C. C.: Analysis on sustainable utilization and exploitation potentiality of shallow groundwater resources in
33 Heze Yellow River flood plain areas, *Shandong Land and Resources*, 30, 43–45, 2014.

34 Massonnet, D., and Feigl, K.: Radar interferometry and its application to changes in the Earth surface, *Reviews of*
35 *Geophysics*, 36, 441–5000, <https://doi.org/10.1029/97RG03139>, 1998.

36 Miller, M. M., and Shirzaei, M.: Land subsidence in Houston correlated with flooding from Hurricane Harvey, *Remote*
37 *Sensing of Environment*, 225, 368–378, <https://doi.org/10.1016/j.rse.2019.03.022>, 2019.

38 Mora, O., Mallorqui, J.J., and Broquetas, A.: Linear and nonlinear terrain deformation maps from a reduced set of
39 interferometric SAR images, *IEEE Transactions on Geoscience and Remote Sensing*, 41, 2243–2253,
40 <https://doi.org/10.1109/TGRS.2003.814657>, 2003.

41 Motagh, M., Shamshiri, R., Haghighi, M. H., Wetzel, H. U., Akbari, B., Nahavandchi, H., Roessner, S. and Arabi, S.:
42 Quantifying groundwater exploitation induced subsidence in the Rafsanjan plain, southeastern Iran, using InSAR
43 time-series and in situ measurements, *Engineering geology*, 218, 134–151, <https://doi.org/10.1016/j.enggeo.2017.01.011>,
44 2017.

1 Parizzi, A., and Brcic, R.: Adaptive InSAR Stack Multilooking Exploiting Amplitude Statistics: A Comparison Between
2 Different Techniques and Practical Results, *IEEE Geoscience and Remote Sensing Letters*, 8, 441–445,
3 <https://doi.org/10.1109/LGRS.2010.2083631>, 2011.

4 Prats-Iraola, P., Scheiber, R., Marotti, L., Wollstadt, S., and Reigber, A.: TOPS Interferometry With TerraSAR-X, *IEEE*
5 *Transactions on Geoscience and Remote Sensing*, 50, 3179–3188, <https://doi.org/10.1109/TGRS.2011.2178247>, 2012.

6 Qiao, G., and Lin, H. J.: Evaluation and analysis of deep groundwater in Heze City, *Shandong Water Resources*, (8), 99–100,
7 2006.

8 Rapantova, N., Grmela, A., Vojtek, D., Halir, J., and Michalek, B.: Groundwater flow modeling applications in mining
9 hydrogeology, in: *IMWA Symposium 2007: Water in Mining Environments*, Cagilari, Italy, 27–31 May 2007, 349–353,
10 2007.

11 Samiei-Esfahany, S.: Exploitation of distributed scatterers in synthetic aperture radar interferometry, PhD thesis, Delft
12 University of Technology, Netherlands, 2017.

13 Shamshiri, R., Nahavandchi, H., Motagh, M., and Hooper, A.: Efficient ground surface displacement monitoring using
14 sentinel-1 data: integrating distributed scatterers (DS) identified using two-sample t-test with persistent scatterers (PS),
15 *Remote Sensing*, 10, 794, <https://doi.org/10.3390/rs10050794>, 2018.

16 Shandong Provincial Bureau of Statistics.: *Shandong Statistical Yearbook*, Beijing, China Statistics Press, China, 2010–2019.

17 Sousa, J. J., Hooper, A. J., Hanssen, R. F., Bastos, L. C., and Ruiz, A. M.: Persistent Scatterer InSAR: A comparison of
18 methodologies based on a model of temporal deformation vs. spatial correlation selection criteria, *Remote Sensing of*
19 *Environment*, 115, 2652–2663, <https://doi.org/10.1016/j.rse.2011.05.021>, 2011.

20 Wang, H. Q.: Mining subsidence monitoring around Longgu coal mine based on remote sensing, *Advanced Materials*
21 *Research*, 1010–1012, 489–495, <https://doi.org/10.4028/www.scientific.net/AMR.1010-1012.489>, 2014.

22 Wang, H. W., Jiang, Y. D., Xue, S., Mao, L. T., Lin, Z. N., Deng, D. X., and Zhang, D. Q.: Influence of fault slip on
23 mining-induced pressure and optimization of roadway support design in fault-influenced zone, *Journal of Rock mechanics*
24 *and Geotechnical Engineering*, 8, 660–671, <https://doi.org/10.1016/j.jrmge.2016.03.005>, 2016.

25 Wang, Y., Zhu, X. X., and Bamler, R.: Retrieval of phase history parameters from distributed scatterers in urban areas using
26 very high resolution SAR data, *ISPRS Journal of Photogrammetry and Remote Sensing*, 73, 89–99,
27 <https://doi.org/10.1016/j.isprsjprs.2012.06.007>, 2012.

28 Wessel, B., Huber, M., Wohlfart, C., Marschalk, U., Kosmann, D., and Roth, A.: Accuracy assessment of the global
29 TanDEM-X Digital Elevation Model with GPS data, *ISPRS Journal of Photogrammetry and Remote Sensing*, 139,
30 171–182, <https://doi.org/10.1016/j.isprsjprs.2018.02.017>, 2018.

31 Xu, J. Y., Mao, L., Zhang, T., and Wang, Z. S.: The development and utilization of water resources and security assurance
32 planning study in Heze City, *China Population, Resources and Environment*, 27, 200–203, 2017.

33 Xu, S. Y., Zhang, Y. B., Shi, H., Wang, K., Geng, Y. P., and Chen, J. F.: Physical Simulation of Strata Failure and Its Impact on
34 Overlying Unconsolidated Aquifer at Various Mining Depths, *Water*, 10, 650–667, <https://doi.org/10.3390/w10050650>,
35 2018.

36 Xue, Y. Q., Zhang, Y., Ye, S. J., Wu, J. C., and Li, Q. F.: Land subsidence in china, *Environmental Geology*, 48, 713–720,
37 <https://doi.org/10.1007/s00254-005-0010-6>, 2005.

38 Yague-Martinez, N., Prats-Iraola, P., Rodriguez, G. F., Brcic, R., Shau, R., Geudtner, D., Eineder, M., and Bamler, R.:
39 Interferometric Processing of Sentinel-1 TOPS Data, *IEEE Transactions on Geoscience and Remote Sensing*, 54,
40 2220–2234, <https://doi.org/10.1109/TGRS.2015.2497902>, 2016.

41 Yang, S. Y., Yang, H. C., Jing, C. Q., Yue, X. L., and Jie, J.: Comprehensive Control of the Coal Mine Subsidence Area: A
42 Case of the Subsidence Area of Chenman Village in Heze of Shandong Province, *China Population, Resources and*
43 *Environment*, 20, 194–196, 2010.

44 Yu, C. J., Jia, P. Y., Lv, S. G., Yuan, X. A., and Zang, X. L.: Analysis of shallow groundwater in Heze city, *Shandong Water*

- 1 Resources, (4), 14–15, 2001.
- 2 Yue, J. G.: Analysis on the current situation and causes of land subsidence along the Lunan high speed railway, Railway
3 Investigation and Surveying, (2), 60–65, 2020.
- 4 Zhang, H., Dong, M., Ma, J., Liu, Y. H., and Liu, K.: Relationship between the deep groundwater exploitation and land
5 subsidence in Changyi district of Shandong province, China Earthquake Engineering Journal, 40, 214–218,
6 <https://doi.org/10.3969/j.issn1000-0844.2018.Supp.214>, 2018.
- 7 Zhang, L. L.: Study on land subsidence prevention and control along the Jingjiu Railway (Shandong Section), PhD thesis,
8 China University of Geosciences (Beijing), Beijing, China, 2013.
- 9 Zhang, Q. Y., Li, Y. S., Zhang, J. F., and Luo, Y.: InSAR Technique Applied to the Monitoring of the Qinghai-Tibet Railway,
10 Natural Hazards and Earth System Sciences, 19, 2229–2240, <https://doi.org/10.5194/nhess-19-2229-2019>, 2019.
- 11 Zhang, Y. H., Underschultz, J., Langhi, L., Mallants, D., and Strand, J.: Numerical modelling of coal seam depressurization
12 during coal seam gas production and its effect on the geomechanical stability of faults and coal beds, International Journal
13 of Coal Geology, 195, 1–13, <https://doi.org/10.1016/j.coal.2018.05.008>, 2018.
- 14 Zhu, C. G., Wang, Z. S., Li, P. X., Motagh, M., Zhang, L. Y., Jiang, Z. L., and Long, S. C.: Retrieval and Prediction of
15 Three-Dimensional Displacements by Combining the DInSAR and Probability Integral Method in a Mining Area, IEEE
16 Journal Of Selected Topics In Applied Earth Observations And Remote Sensing, 13, 1206–1217,
17 <https://doi.org/10.1109/JSTARS.2020.2978288>, 2020.